



Liu Weiguang (Orcid ID: 0000-0001-9561-7385)
Wang Guiling (Orcid ID: 0000-0002-9744-2563)
Yu Miao (Orcid ID: 0000-0002-1353-9406)
Chen Haishan (Orcid ID: 0000-0002-2403-3187)
Jiang Yelin (Orcid ID: 0000-0003-2676-575X)

Multi-Model Future Projections of the Regional Vegetation-Climature System over East Asia: Comparison between two ensemble approaches

Weiguang Liu^{1,2}, Guiling Wang^{2*}, Miao Yu^{1*}, Haishan Chen¹, and Yelin Jiang²

¹Key Laboratory of Meteorological Disaster, Ministry of Education/International Joint Research Laboratory on Climate and Environment Change /Collaborative Innovation Center on Forecast and Evaluation of Meteorological Disasters, Nanjing University of Information Science & Technology, Nanjing 210044, China

²Department of Civil and Environmental Engineering, and Institute of the Environment, University of Connecticut, Storrs, CT 06269, USA

Corresponding authors: Guiling Wang (guiling.wang@uconn.edu), Miao Yu (yum@nuist.edu.cn)

Key Points:

- Two ensemble approaches are used to project the future vegetation-climate changes over East Asia
- Projected changes over Northeast China are highly sensitive to the GCM-derived boundary conditions
- Vegetation feedback has significant impacts on winter temperature over Northeast China and Tibetan Plateau due to albedo effects

This article has been accepted for publication and undergone full peer review but has not been through the copyediting, typesetting, pagination and proofreading process which may lead to differences between this version and the Version of Record. Please cite this article as doi: 10.1029/2019JD031967

Abstract

This study compares two ensemble methods, pseudo global warming (PGW) and multi-model ensemble mean (MME), in evaluating future vegetation-climate changes and feedback over East Asia using a regional model driven with boundary conditions derived from historical and RCP8.5 runs of four global models. Over most of the domain, MME and PGW produce similar future climate changes, except for two regions: over Northeast Asia, MME projects less winter warming and less increase of summer precipitation than PGW; over North China Plain, MME projects greater increase of summer precipitation than PGW. Both PGW and MME project greater leaf area index (LAI) and expansion of tree coverage at the expense of grass over most of the domain due to elevated CO₂ concentration and climate change. However, over Northeast China, PGW and three ensemble members project an increase of temperate trees at the expense of boreal trees or grass and a decrease of LAI, and one ensemble member projects a loss of forest to grassland. Both PGW and MME identify two hotspots of vegetation-temperature feedback, including the Northeast China where the projected loss of boreal evergreen forest causes a significant winter cooling (which offsets a major portion of GHG-induced warming), and the Tibetan Plateau where the projected LAI increase and vegetation expansion lead to a significant winter warming through reduced albedo. The vegetation feedback impact on precipitation is similar between the two approaches, including a significant wet signal in a belt between 30–40°N during winter and over the Tibetan Plateau during summer.

Keywords: Vegetation-climate interactions; Multi-model ensemble; Climate change; East Asia

Plain Language Summary

Climate is undergoing severe changes. Climate simulation and projections from global climate models suffer from coarse resolution and model dependence, especially for the East Asia region. In this study, we assess multi-model ensemble projections of the East Asian vegetation-climate changes using a regional model driven with boundary conditions from multiple global models. Two ensemble approaches are used, the traditional multi-model ensemble mean (MME) that is based on unweighted average of the four runs driven with individual global models, and the reanalysis-based pseudo global warming (PGW) that derives the regional model's boundary conditions by adding the 4-model average of future changes to the boundary conditions from the reanalysis data. PGW and MME produce a similar future climate change signals over most of the model domain except for the Northeast China, North China and India region. Both PGW and MME identify two hotspots of vegetation-temperature feedback, including the Northeast China with significant winter cooling due to forest loss and the Tibetan Plateau with significant winter warming due to LAI increase and vegetation cover expansion.

1 Introduction

As the global surface temperature continues to rise with the increase of greenhouse gas (GHG) concentration, so does the need for regional climate change assessment to support the development of climate adaptation and mitigation strategies. This is especially critical for densely populated regions such as the East Asian Monsoon region (e.g., Cai et al., 2017). However, regional-scale climate change projections from global models are often deemed unreliable (e.g., Xie et al., 2015), and are subject to a large degree of model uncertainty (e.g., Hall 2014; Jiang and Tian, 2012; He and Zhou, 2015). Regional climate models (RCMs) inherit atmospheric circulation uncertainties from general circulation models (GCMs) and do not address this issue. The multi-model ensemble mean (MME) approach is usually used to reduce the uncertainties of future climate change projections from both regional and global models (Collins et al., 2012; Erfanian et al., 2016; Gao et al., 2018; Wu et al., 2020). However, to account

for uncertainties originating from both the regional model and the driving global model, MME approach for regional climate projections needs to include multiple RCMs driven by different GCMs (White and Toumi, 2013; Schaller et al., 2011; Means et al., 2012; Giorgi et al., 2012; Erfanian et al., 2016, 2017), and the large number of simulations is computationally inhibiting. Moreover, the conventional MME mean creates physical inconsistency among different climate variables and diminishes the magnitude of inter-annual variability.

To overcome the challenges of the conventional MME approach, alternative ensemble approaches have been developed. For example, Erfanian et al. (2017) developed an Ensemble-based Reconstructed Forcing (ERF) method for regional climate projections as an alternative. The ERF approach involves a single historical-vs-future pair of RCM integration, where lateral boundary conditions (LBCs) for the RCM historical simulation were derived from the multiple-model ensemble mean of the GCM historical runs and LBCs for the RCM future projection were derived from the multi-model ensemble mean of the GCM future runs. While the ERF approach can dramatically reduce the computational cost while attaining a desirable level of performance in simulating the mean climate, inter-annual variability is dampened and important inter-annual climate phenomena (e.g., El Nino) are not captured due to the use of ensemble mean LBCs. Another approach based on the concept of pseudo global warming (PGW) derives the RCM historical LBCs from reanalysis data, and derives the RCM future LBCs by summing the 6-hourly reanalysis data and the differences between GCMs' historical and future climates (Kawase et al., 2009; Xu et al., 2018). In order to quantify the uncertainty around the mean climate using the PGW method, the climatological increments estimated by GCM simulations were statistically analyzed using the Singular Vector Decomposition (SVD) to create multiple model LBCs for the RCM future simulations (Wakazuki and Rasmussen 2015). With the PGW approach, the inter-annual variability in both the historical and future RCM simulations originates from the reanalysis data. In this study we assess future climate and vegetation changes in Asia using the PGW approach and compare with the conventional MME approach.

Future climate changes are projected to induce substantial changes of the terrestrial ecosystem (Cramer et al., 2001; Diffenbaugh and Field, 2013; Zhu et al., 2016; Liu et al., 2019). Because of the rising GHG concentration and increasing temperature, the Earth is greening up globally, with the CO₂ fertilization effects as the dominant driver in the Tropics and with the warming effect as the dominant driver in cold regions including high latitudes and the Tibetan Plateau (Zhu et al., 2016); leaf area index (LAI) changes simulated by dynamic global vegetation models (DGVMs) driven with projected future climate indicated that the observed greening trend will continue into the future (Sitch et al., 2008; Yu et al., 2014; Gang et al., 2017). Moreover, vegetation composition is also expected to change. Using different versions of DGVM in the Community Land Model (CLM-DGVM) driven with climate projections from multiple GCMs, Alo and Wang (2008) and Yu et al. (2014) both found a poleward spread of temperate and boreal forests at the northern high latitudes and a shift from evergreen to drought deciduous trees in the Tropics. Yu et al. (2014) showed that the competition between climate change and CO₂ fertilization effects leads to large uncertainties in projecting future vegetation changes in the Tropics. Using a Comprehensive Sequential Classification System and the segmentation model driven with climate change from 33 GCMs under four Representative Concentration Pathways (RCPs), Gang et al. (2017) exhibited that forest and desert would expand globally at the cost of grassland, particularly in the Northern Hemisphere. Regionally, diverse changes of vegetation may occur, with the direction and magnitude of changes depending on both climate mean and extremes (Yu et al., 2019). For example, Gao et al. (2017) found spatially heterogeneous responses to past climate change in northern China, with the Northwest and Northeast differing in the primary climate driver for past vegetation trends, based on a positive precipitation-vegetation correlation over Northwest China and the Northeast China Plain and a negative temperature-vegetation correlation over the rest of Northeast China.

Climate-induced vegetation changes can influence land-atmosphere flux exchanges thus further modifying regional climate (Bonan 2008; Alkama and Cescatti, 2016). The local impacts of vegetation-atmosphere interactions are dependent on the geographical position and climatology background (Nemani et al., 2003; Swann et al., 2016; Lee et al., 2011). Xue et al. (2010) illustrated that globally monsoon regions are experiencing the strongest vegetation biophysical process impacts, and East Asia is one of the most influenced regions. Notaro et al. (2011) found that monsoon response to a reduction of vegetation cover is region dependent, with a delay of monsoon onset over Australia and an advance over China and Southwest United States. Several modeling and observational studies focusing on North China and East China suggested that the increase of tree coverage may have been the cause for an increase of precipitation and evapotranspiration and a decrease of temperature during summer (Ma et al., 2013; Yu et al., 2013; Wei et al., 2017), but spatial heterogeneity in climate response to land cover changes can be substantial (Niu et al., 2019). In addition to prescribed vegetation cover changes, interactions between dynamic vegetation and regional climate are also important and the mechanistic effects can be highly region-dependent (Dan et al., 2015; Yu et al., 2016; Shi et al. 2019).

This study focuses on evaluating future changes of climate and vegetation over East Asia (especially China) using a synchronously coupled regional climate-vegetation model and compares two different ensemble approaches to account for uncertainties originating from global models. Section 2 describes the model, data and experimental design, and results are presented in Section 3. Section 4 discusses the existing issues and gives the main conclusions.

2 Method

The model used in this study is the Regional Climate Model Version 4.3.4 (RegCM4.3.4) from the International Centre for Theoretical Physics (Giorgi et al., 2012) synchronously coupled with the Community Land Model version 4.5 (CLM4.5, Oleson et al., 2010, 2013) including the carbon-nitrogen (CN) and dynamic vegetation (DV) sub-models (RegCM-CLM-CNDV, Wang et al., 2016). The CN and DV sub-models can be turned on or off depending on specific applications. With the CN-DV component turned on, the full RCM-CLM-CNDV simulates the regional climate and vegetation distribution, structure, and density; with the CN-DV component turned off, the RCM-CLM simulates regional climate based on static vegetation with distribution and phenology prescribed according to the Moderate Resolution Imaging Spectroradiometer (MODIS) data, including the fractional coverage of different plant functional types (PFTs) and seasonally varying LAI (Lawrence and Chase, 2007; Lawrence et al., 2011).

Both static vegetation (i.e., RCM-CLM) and dynamic vegetation simulations (i.e., RCM-CLM-CNDV) are conducted from 1979 to 1999 for the historical period, and from 2079 to 2099 for the RCP8.5 future scenario. To derive the initial carbon, nitrogen, and vegetation conditions for RCM-CLM-CNDV, we followed the approach of Wang et al. (2016) and spun up the offline CLM-CNDV model driven by atmospheric forcing simulated by RCM-CLM for each of the period, with CO₂ concentrations of 353.8 and 850.0 ppm for historical and RCP8.5 simulations, respectively; the resulting equilibrium state (after ~300 years of spinning up) was used to initialize RCM-CLM-CNDV in the corresponding simulation. To minimize the “initial shock” effect, each RCM-CLM-CNDV run (historical or future) cycled through the same 20-year LBC forcing twice. That is, the first 1979-1999 run was initialized by output from the offline CLM-CNDV, and the second 1979-1999 simulation was initialized by output from the last year of the first. Output from the second 20 years are used for results analysis. This experimental design entails historical and future runs using both RCM-CLM-CNDV and RCM-CLM, where RCM-CLM-CNDV projects future changes in both climate and vegetation with

the two synchronously coupled and RCM-CLM projects future climate changes with vegetation fixed at present-day observed conditions. While future changes projected by RCM-CLM-CNDV runs are the primary focus of our results analysis, comparison with climate changes projected by RCM-CLM runs enables us to quantify the impact of dynamic vegetation-climate feedback.

The model domain covers approximately 10°-60°N, 70°-140°E with a horizontal resolution of 50 km, and the top of the model atmosphere is set to 50hPa with 18 sigma levels. The model physics parameterizations include the radiative transfer scheme from Community Climate Model version 3 (Kiehl et al., 1996), the cumulus convection scheme from Emanuel (1991) and planetary boundary layer scheme from Holtslag et al. (1990). More details of the coupled model can be found in Wang et al. (2016) and Shi et al. (2019). Model performance in simulating the historical climate and vegetation will be evaluated against the PFT and LAI data from MODIS, and 2-m air surface temperature and precipitation from Climatic Research Unit (“CRU” hereafter; Harris et al., 2014). Another gridded observational data set CN05.1 (Wu and Gao, 2013) is included for evaluating model performance inside China. Both observation and model output are remapped to 0.5° grids to facilitate their comparison, and the units of the temperature and precipitation are converted into °C and mm day⁻¹, respectively.

To account for uncertainties originated from GCMs, outputs from historical and RCP8.5 future scenario runs (Moss et al., 2010) of four GCMs (Table 1) are used to derive LBCs for the regional model. Two different ensemble approaches are used: the conventional MME approach and the reanalysis-based pseudo global warming downscaling method (“PGW” hereafter; Kawase et al., 2009; Xu et al., 2018). MME includes four pairs of historical-vs-future regional runs, in which the historical and future LBCs from each individual GCM are used to drive the regional model and the unweighted average of the regional model outputs are used for comparison between historical and future climates. The PGW ensemble approach entails only one pair of historical-vs-future RCM runs, where the historical LBCs are derived from the ERA-Interim data (“ERA” hereafter) and future LBCs are constructed by adding the GCM-projected LBC changes (i.e., in temperature, surface pressure, humidity and wind) to the historical LBCs (from ERA reanalysis):

$$PGW(ERA_F) = ERA_H + \overline{MME_F} - \overline{MME_H} \quad (1)$$

where ERA_H is the historical LBCs from the 6-hourly reanalysis data, $PGW(ERA_F)$ represents the constructed future LBCs at 6-hourly intervals based on ERA, $\overline{MME_F}$ and $\overline{MME_H}$ are the 20-year climatology of 4-GCM ensemble mean of LBCs at 6-hourly intervals for the historical (i.e., 1980–1999) and future (i.e., 2080–2099) periods, respectively. Because reanalysis and GCMs use different calendars, all of the LBCs are converted to the same “no-leap” calendar.

3 Results

3.1 Model Performance for Present-day Climate and Vegetation

Shi et al. (2019) documented in detail the performance of the RCM-CLM and RCM-CLM-CNDV models in simulating the present-day climate in China when driven with reanalysis LBCs, and found a good agreement between the model present-day climate and observations. As the focus of this study is the comparison between the two different ensemble approaches to future projections, only a brief description of model comparison with observations is provided here.

Figure 1 shows the RCM-CLM-CNDV model biases for the historical climate of MME and ERA (for PGW). Although the MME can reduce the model biases caused by the GCM-derived LBCs to some extent, strong cold biases remain over the majority of the domain with much stronger biases during winter (DJF) than summer (JJA; Figs. 1a-d). The cold biases from the ERA-driven (Figs. 1a, c) and MME (Figs. 1b-d) historical experiments are similar. These

biases result primarily from biases related to the RCM model structure. The cold biases are also consistent with results from previous studies (Gao et al., 2006, 2017; Shi et al., 2017; Ali et al., 2015; Notaro et al., 2017). Relative to CN05.1 using 2400-station data from China, CRU overestimates temperature especially in winter (Fig. S1). For precipitation, the performance of the MME approach over most of the domain is also similar to the one driven with ERA-based LBCs, with overestimation in arid or semi-arid regions and underestimation in humid or semi-humid regions (Figs. 1e-h). Exceptions are found during summer over North China Plain and Northeast China where MME produces a strong dry biases while biases in the ERA-driven historical run are mostly negligible (Figs. 1e, g). Over the majority of the domain, most of individual MME members (i.e., 3-4 out of four individual GCM-driven experiments) agree with the MME mean in the direction of the biases.

To evaluate the performance of the dynamic vegetation model in simulating the natural potential vegetation during the historical period, Figure 2 exhibits the vegetation coverage observed from MODIS and simulated by the model. Due to the inability of RCM-CLM-CNDV to model managed vegetation (i.e., crops; Fig. 2j), the proportion of bare ground and natural vegetation is overestimated: over the western part of the domain, especially over India, the bare ground (Figs. 2a-c) is overestimated and LAI underestimated relative to the MODIS data (Figs. 2k-m); over the majority of the eastern part of the domain, the coverage of woody plants (i.e., tree and shrub; Figs. 2d-f) is overestimated, which partly explains the larger-than-observed LAI in the model (Figs. 2k-m). On the other hand, due to signal saturation, high LAI is likely underestimated in MODIS (Murray-Tortarolo et al., 2013). In general, the MME and ERA-driven historical simulations produce a similar spatial distribution of vegetation type and density, with differences over Northeast China and the neighboring North China region. Over these regions, the ERA-driven RCM-CLM-CNDV overestimates tree coverage (Fig. 2e) and the MME overestimates grasses coverage (Fig. 2i), indicating that the local vegetation and climate might be highly sensitive to LBCs. This will be further analyzed in subsection 3.3.

3.2 Surface Climate Change

RCM-CLM-CNDV and RCM-CLM project similar climate changes over most of the domain, except for regions with strong vegetation feedback to climate. Here we assess the surface climate changes based on output from the RCM-CLM-CNDV experiments (Figure 3), and will describe the dynamic vegetation feedback to regional climate in subsection 3.4. RCM-CLM-CNDV driven with individual GCM LBCs projects significant warming across the domain, but the magnitude of the projected warming differs among the ensemble members. MME and PGW approaches produce similar magnitude and spatial patterns of future warming over most of the domain (Figs. 3a, b, d, e); the differences between PGW and MME projections are mainly over arid and semi-arid regions (e.g., the western and northeastern part of the domain), and the differences in summer (Fig. 3f) are weaker than in winter (Fig. 3c). Over Northeast China during winter (Fig. 3c), the large differences between MME and PGW as well as among different MME members might be caused by the diverse response of vegetation cover in this region to climate change.

For most the region, more precipitation is projected except the southeastern part in the winter. Although the magnitudes of future precipitation changes are smaller in DJF (Figs. 3g-h) than in JJA (Figs. 3j-k), the changes in the northern part are statistically significant because of the rather small precipitation variability. In DJF, both the PGW (Fig. 3g) and MME (Fig. 3h) approaches project a decrease of precipitation over Southeast China and an increase over the rest of the domain. In JJA, precipitation is projected to increase over the Southeast China by most simulations; over the North China Plain, PGW projects a mixed response of precipitation with some areas of strong decrease (Fig. 3j) while MME projects a strong, spatially coherent increase with a high level of consensus among the ensemble members (Fig. 3k-l). The

regions where precipitation difference between PGW and MME are significant coincide with those of significant temperature differences.

In addition to the mean climatology, the inter-annual variability is also an important factor for the East Asian monsoon region. Take the East Asian summer monsoon region (EASMR; Figure 2a) from Li et al., (2019) as an example, Table 2 lists the spatially averaged mean and inter-annual standard deviation of JJA temperature and precipitation and their future changes. For the historical period, it is clear that the ERA-driven experiments have more realistic temperature ($0.65\text{ }^{\circ}\text{C}$) and precipitation (1.48 mm day^{-1}) variability than the MME mean ($0.38\text{ }^{\circ}\text{C}$ and 0.70 mm day^{-1} , respectively). PGW and MME project similar magnitude of the temperature changes, and their differences in projecting precipitation changes are larger. Not surprisingly, MME reduces the inter-annual variability of both temperature and precipitation, leading to a much smoother time series and an unusually low inter-annual variability than individual MME members or the PGW approach. For temperature based on both ensemble approaches and based on each MME member, the projected changes in the mean (about $5.2\text{--}5.4\text{ }^{\circ}\text{C}$) far exceeds both the inter-annual variability and the model-related uncertainties. For precipitation, while a clear increase is projected based on all approaches, the magnitude of the increase projected by each ensemble member is small (although statistically significant) relative to the large magnitude of internal variability and model uncertainties.

It is notable that the CCSM4-driven historical temperature ($24.63 \pm 0.69\text{ }^{\circ}\text{C}$) is highest and FGOALS-g2-driven future temperature ($27.13 \pm 0.71\text{ }^{\circ}\text{C}$) is the lowest; the GFDL-driven experiments produce the lowest historical temperature ($22.99 \pm 1.01\text{ }^{\circ}\text{C}$) and the highest future temperature ($30.37 \pm 0.91\text{ }^{\circ}\text{C}$). Collectively, these serve as a reminder that strong performance in simulating the present-day climate does not mean more realistic future projections.

3.3 Projected Vegetation Changes

For future vegetation changes over most of the model domain, both the PGW and MME approaches project a mild increase of woody plants coverage and a compensating decrease of grass coverage and bare ground (Figure 4). The magnitude of the projected vegetation changes are the largest over Tibetan Plateau and most of northern China. Notable differences between PGW and MME are found over two regions: over India where MME projects a greater expansion of tree coverage into areas that are historically grassland or bare ground, and over the Northeastern portion of the domain where MME projects more bare ground and grass coverage and less woody plants coverage than PGW. In addition to vegetation cover changes, LAI is also projected to increase over most of the domain (Figs. 4g-h) except for the arid and semi-arid regions (e.g., Northwest China). The general increase of woody plant coverage and LAI are primarily a result of the CO_2 fertilization effects dominant over climate change impact. A notable exception from the greener and denser projection is found in MME over the Northeast China where woody plants are projected to lose the competition to grass in the future (Figs. 4d, f); in PGW, such a signal for grass-vs-tree competition is projected for regions much further north (and appears to extend beyond the model domain).

Considering the remarkable disparities between the two approaches in surface climate (Figs. 1g-h) and vegetation (Figs. 2d-f) over Northeast China and India, the spatially averaged vegetation coverage fraction for these regions are shown in Figure 5. For Northeast China (Figure 5a), the model driven with all LBCs can reproduce the observed spatial distribution of vegetation type, including boreal needleleaf evergreen tree, boreal broadleaf deciduous tree, arctic C3 grass and bare ground, but the magnitudes differ among the LBCs. The historical simulations driven with ERA and three of the four GCMs (e.g., FGOALS-g2, GFDL-CM3 and HadGEM2-ES, Fig. 3a) produce considerable tree coverages (e.g., boreal needleleaf evergreen trees and boreal broadleaf deciduous trees), but the historical simulation driven with CCSM4 produces less tree coverage and much more bare ground and arctic C3 grass instead. In the

future, the CCSM4-driven projection produces a moderate forest expansion and FGOALS-driven projection produces a substantial forest loss, while both the GFDL- and HadGEM2-driven projections suggest a shift in the dominant tree type from boreal needleleaf evergreen to temperate broadleaf deciduous trees with little change in the total tree coverage. Collectively, these changes lead to a loss of tree coverage in the MME ensemble mean. In the FGOALS-driven projection, the evergreen trees are replaced with grasses, and the temperate broadleaf deciduous tree coverage shrinks to the Korean peninsula (figures not shown); in all other projections (driven by CCSM4, GFDL, HadGEM2, and PGW), the temperate trees would either win the competition either against grass (in the CCSM4-driven projection) or against the boreal needleleaf evergreen trees that are vulnerable to the projected increase of summer heat (in the projections driven by GFDL, HadGEM2, and PGW).

The high degree of model dependence of simulated vegetation in Northeast China (Figure 5a) result from the model's climate dependence on LBCs. Figure 6a presents the seasonal cycle of climate variables averaged over the Northeast China from RCM-CLM simulations with static vegetation (which is close to the climate of RCM-CLM-CNDV over most of the domain). For the historical period, temperature in RCM-CLM (Fig. 6a) has a large inter-model range, reaching ~ 8 °C in summer (between the highest mean temperature in the model driven with CCSM4 LBCs and lowest in the model driven with GFDL LBCs); results from MME and ERA-driven simulation are similar, reflecting the effectiveness of ensemble mean in reducing LBC-induced temperature biases. On the other hand, precipitation (Fig. 6a) are more heavily influenced by the RCM circulation field than LBCs, and its largest inter-model range (which occurs in summer) is ~ 0.5 mm/day; meanwhile, precipitation is subject to stronger internal variability than temperature, which underlies the large disparity between MME and the ERA-based historical simulation. ET is strongly influenced by air surface temperature and shows a model-dependence similar to temperature, with the highest ET in CCSM4- and lowest in FGOALS- and GFDL-driven simulations (Fig. 6a). Both the precipitation and temperature differences contribute to soil moisture differences among different ensemble members. For example, among the four simulations driven with GCM LBCs, the CCSM4-driven simulation has the lowest precipitation, highest ET, and therefore driest soil (Fig. 6) during the growing season, which favors grass over trees; in addition, higher temperature can induce heat stress for boreal trees and ultimately cause boreal forests to lose the competition to grass in the CCSM4-driven simulation (which then influences the MME results). For the RCP8.5 future experiments, the warming magnitudes from FGOALS-g2 is the weakest in winter (Fig. 6a), which is not sufficient to push the future temperature past the threshold for temperate broadleaf deciduous forests to establish and survive over some regions (Fig. 5a), thus the boreal grass dominates in the future. In other future change experiments, an extensive coverage of temperate broadleaf deciduous trees are projected for the future because the annual coldest monthly air temperature (Fig. 6a) is projected to exceed the survival threshold (-17 °C) for temperate trees.

For vegetation over India, PGW, MME, and three of the four ensemble members all project quite similar historical vegetation and future vegetation changes (Fig. 5b). The experiment driven by FGOALS-g2 produces much more tropical broadleaf deciduous trees instead of bare ground, contributing to the differences between MME and PGW. The uniqueness of results from the experiments driven with FGOALS-g2 likely results from the very low projected temperature (lower than any other ensemble members) (Fig. 6b) that is not high enough to induce heat stress. The changes over most of the other regions are qualitatively similar to Tibetan Plateau (Fig. 5c), where the vegetation coverage changes are gradual and consistent among PGW, MME and 4 MME members.

Despite the differences among the models driven with different LBCs and between the two ensemble approaches in projecting tree coverage changes over Northeast China, PGW, MME mean and all individual members of the MME are in agreement on a projected decrease

of LAI over Northeast China (Figs. 4g-h), indicating that the CO₂ fertilization effects cannot offset the climate change induced browning in this region. Apart from few bare ground increase (Figs. 4b, 5a), in most of the projections, the reduction of LAI is dominated by the loss of winter foliage due to the transition from evergreen to deciduous trees (Figure 5a); in the CCSM-driven projection, the LAI reduction is dominated by a decrease of vegetation density during the growing season, despite of the conversion from grass to woody plants. In addition to the effect of plant functional type changes, both the projected heat and water stress contribute to the decrease of LAI during the growing season.

3.4 Impacts of Vegetation Dynamics

The impacts of dynamic vegetation feedback on projected future temperature and precipitation changes are exhibited in Figure 7. Based on both PGW and MME approaches, the impact of dynamic vegetation feedback on DJF precipitation features a weak but statistically significant wet signal along 30°N-35°N of the China domain (Figs. 7e-f), resulting from the projected increase of LAI across most of the domain. For JJA precipitation, the impact of vegetation dynamics is stronger but does not pass the statistical significance test across the domain except for part of the Tibetan Plateau (Figs. 7g-h) where the projected vegetation expansion tends to promote precipitation.

Relative to the precipitation signal, significant impact of dynamic vegetation feedback on temperature is simulated over a larger portion of the domain in both PGW and MME. During summer across most of the domain based on both ensemble approaches, vegetation feedback leads to a cooling signal (Figs. 7c-d) as a result of projected LAI increase enhancing evapotranspiration (Figs. 8g-h); during winter, there are substantial differences between PGW and MME along 32.5°N over the Tibetan Plateau region, around the Northeast China, and over part of India (Figs. 7a-b), which is consistent with the substantial differences between the two ensemble approaches in projecting future vegetation changes.

Over the Northeast China region, both approaches produce a strong cooling effects during winter (Figs. 7a-b) due to the foliage loss caused by the projected loss of boreal needleleaf evergreen trees, with a much larger spatial extent of this cooling signal based on the MME approach. The cooling is caused by the significant radiative effects of albedo increase (Fig. 9a) due to the reduction of wintertime LAI and partial loss of vegetation cover. Indeed, the vegetation feedback signal for temperature is similar to that for absorbed solar radiation (Figs. 8a-b). In summer, both the albedo effect (cooling) and the evapotranspiration effect (warming) of the LAI reduction are important (Figs. 8c, d, g, h), which offset each other. As a result, the vegetation feedback effect on summer temperature is negligible (Figs. 7c-d).

Over the India region, similar to the projected expansion of vegetation cover, the vegetation feedback to temperature has a winter cooling effect in MME mean due primarily to the increased evapotranspiration in the outlier model FGOALS-g2 model (Fig. 9b); PGW and most of MME members agree with the direction of the temperature signals. Over the Tibetan Plateau, the PGW approach produces an extremely strong winter warming (Fig. 7a) due to increase of vegetation cover. However, the winter warming signal based on the MME approach is much weaker (Fig. 7b), which is a result of a strong albedo-induced warming in the HadGEM2-driven projection (Fig. 9c) moderated by either a cooling signal or no-change from the other three ensemble members (driven by GFDL-CM3, CCSM4, and FGOALS-g2) (Fig. 7b).

Given the long snow season in the present-day climate of both Northeast China and Tibetan Plateau regions, the impact of vegetation feedback on snow depth was also analyzed (Figure 10). No significant impacts are found over Northeast China, but strong and consistent reduction of snow depth are projected by both PGW and MME over Tibetan Plateau (Figs. 10a-b). The decrease of snow depth and snow duration (Fig. 10c) leads to a lower surface

albedo, which further enhances the vegetation albedo effect on surface solar radiation absorption (Fig. 9c) and the resulting warming over Tibetan Plateau.

4 Conclusions and Discussion

This paper investigates the potential dependence of regional climate and vegetation projections on the driving GCMs and on the ensemble approaches. Initial and boundary conditions from multiple sources, including the ERA-Interim reanalysis data and four CIMP5 GCMs, are used to drive a regional climate-vegetation model. Two multi-model ensemble approaches are compared, including the traditional multiple model ensemble mean and reanalysis-based pseudo global warming method. While the traditional MME approach reduces the random errors in individual models thus helping identify the most significant signal of future changes, it also underestimates the inter-annual variability of the regional climate. PGW as an alternative can capture most of the main projected signals without losing the inter-annual variability; however, over regions of strong vegetation-climate feedback, PGW's mean climate may differ substantially from the MME mean.

The two ensemble approaches project similar temperature and precipitation changes, with strong warming and a general wet signal across the domain. The two approaches differ substantially in some regions, over the North China Plain where the MME approach projects a strong wet signal while PGW produces a mixed precipitation signal for summer, over Northeast China and adjacent regions where MME projects a much smaller magnitude of winter warming than PGW, and over western India where MME projects a strong increase of summer precipitation while the signal in PGW is weak and mixed. The different winter warming in Northeast China has to do with the strong response of vegetation in this region especially the loss of forest to grassland in one member of the MME approach. Over the rest of the domain, PGW can replace the MME approach with a much lower computational cost without sacrificing accuracy.

Over the southern part of the East Asia domain, due to the increasing CO₂ concentration and rising temperature, both PGW and MME project a mild "upgrade" of vegetation type (from bare ground to grass and from grass to trees) and a greening trend with increases of LAI. Over the northern part of the domain, both PGW and MME project a browning trend with decreases of LAI due to shifts of vegetation types and growing-season heat stress, but the two approaches differ in projecting the magnitude and spatial extent of the LAI changes and vegetation type shifts, especially over Northeast China. Over Northeast China, of the four MME members, three project a shift from boreal needleleaf evergreen trees to temperate broadleaf deciduous trees, and one outlier projects a loss of forest to grassland. Meanwhile, the projection from PGW is similar to the majority of the MME members.

Both PGW and MME approaches identify Northeast China and the areas to the north and Tibetan Plateau as regions of strong vegetation-temperature feedback during winter. Because evaporative cooling is negligible during winter, the projected reduction of LAI over Northeast China can lead to local cooling due to higher albedo; the projected increase of vegetation coverage and LAI over Tibetan Plateau can increase local temperature due to lower albedo, and this warming effect can be further enhanced by the albedo effect of snow reduction. The significant vegetation feedback is consistent among projections driven by all GCMs over Northeast China and shows a higher degree of model dependence over the Tibetan Plateau.

Findings from this study are subject to model limitations. The dynamic vegetation model coupled with the regional model cannot simulate managed vegetation. Instead, natural potential vegetation is simulated over cropland and pastureland. Within our model domain, the India, North China and Northeast China regions are primarily agricultural land in reality and are simulated to be forest and grassland by the model. This partially contributed to the overestimation of tree coverage and LAI in the historical simulation. The overestimation of LAI from dynamic

vegetation model is in line with results from Murray-Tortarolo et al. (2013) and Anva et al. (2013).

Compared to vegetation projections using offline DGVMs driven with climate from GCMs, which are subject to uncertainties originating from the DGVMs and GCMs, the projections in this study are subject to additional uncertainties and biases related to the structure of the regional climate model as well as the feedback between climate and vegetation, as discussed in previous studies (e.g., Wang et al., 2016; Gao et al., 2016; Shi et al., 2019). For regions where the vegetation-climate feedback is strong, biases in the historical simulation using the coupled model and uncertainties of future projections are expected to be larger than models without vegetation dynamics. However, as shown in Shi et al. (2019), the biases in this particular model for this particular region were at a similar magnitude to those with prescribed vegetation, so the added model capacity was not at the expense of model performance.

Both the MME and PGW ensemble approaches can reduce the uncertainties associated with GCM LBCs. However, when the ensemble size is small, the results of MME and PGW will be affected by the choice of GCMs and one distinctive model may dominate the ensemble mean. Specifically in this study, the overestimation of temperature in CCSM4 plays an important role in the MME present-day climate biases; the large magnitude of warming from GFDL is clearly reflected in the ensemble projections of temperature. This will be less problematic as the ensemble size increases.

Across most of the model domain, Northeast China and the adjacent region of North China Plain are identified in this study as a hotspot of large model uncertainty and high climate and ecosystem sensitivity. In fact, Northeast China region suffered from record-breaking summer heat in 2018 and global warming was found to have increased the probability of such extreme heat in the region by 78% (Zhou et al., 2020). In the context of the model, the high uncertainty and sensitivity in the Northeast China have to do with the fact that maximum temperature in the present-day climate is close to the threshold for the onset of heat stress for boreal evergreen trees and the minimum temperature is close to the survival threshold for temperate deciduous trees. As a result, model biases and projected changes in temperature can likely cause a threshold to be crossed and thus favor a vegetation type that has a leaf phenology different from observations or present-day climate, with especially strong feedback to winter temperature due to the vegetation albedo effect. Specifically, for the present-day simulations, warm bias and dry bias (mainly caused by the driving LBCs) will lead to drier soil and more severe heat stress in the model, which may limit tree growth and leads to underestimation of tree coverage. For the future, warming is strong at mid- to high- latitudes even during summer, and boreal trees are among the most vulnerable biomes under climate change. Because of the projected warming, the coldest temperature will no longer limit the survival and establishment of new PFT types such as temperate broadleaf deciduous tree over Northeast China, and the higher temperature during the summer growing season will cause heat stress that influences all PFTs, leading to lower LAI (vegetation browning). For similar reasons, Tibetan Plateau (where present-day temperature is low due to high altitude) is another region that is sensitive to projected warming. Future projections for this region feature an expansion of temperate broadleaf tree coverage over the present-day bare ground, which leads to a future increase of LAI.

Acknowledgements

The authors thank the two anonymous reviewers for their constructive comments on an earlier version of this paper. This study was made possible by a scholarship from the China Scholarship Council that supported Weiguang Liu's visit to the University of Connecticut. Computational support was made available through an NCAR computing project to the University of Connecticut (UCNN0017). Yu and Chen were supported by the National Natural Science Foundation of China (41575084 and 41625019). Liu acknowledges funding support

by the Postgraduate Research and Practice Innovation Program of Jiangsu Province (KYCX18_1013). We thank the World Climate Research Programme's Working Group on Coupled Modeling, which is responsible for CMIP. For CMIP5, the US Department of Energy's Program for Climate Diagnosis and Intercomparison provides coordinating support and led development of software infrastructure in partnership with the Global Organization for Earth System Science Portals. All the CMIP5 model output was obtained through <https://esgf-node.llnl.gov/search/cmip5/>.

References

1. Ali, S., Dan, L., Fu, C., & Yang, Y. (2015). Performance of convective parameterization schemes in Asia using RegCM: simulations in three typical regions for the period 1998–2002. *Advances in Atmospheric Sciences*, 32(5), 715-730. <https://doi.org/10.1007/s00376-014-4158-4>.
2. Alkama, R., & Cescatti, A. (2016). Biophysical climate impacts of recent changes in global forest cover. *Science*, 351(6273), 600-604. <https://doi.org/10.1126/science.aac8083>.
3. Alo, C. A., & Wang, G. (2008). Potential future changes of the terrestrial ecosystem based on climate projections by eight general circulation models. *Journal of Geophysical Research: Biogeosciences*, 113(G1). <https://doi.org/10.1029/2007jg000528>.
4. Anav, A., Murray-Tortarolo, G., Friedlingstein, P., Sitch, S., Piao, S., & Zhu, Z. (2013). Evaluation of Land Surface Models in Reproducing Satellite Derived Leaf Area Index over the High-Latitude Northern Hemisphere. Part II: Earth System Models. *Remote Sensing*, 5(8), 3637-3661. <https://doi.org/10.3390/rs5083637>.
5. Bonan, G. B. (2008). Forests and climate change: forcings, feedbacks, and the climate benefits of forests. *Science*, 320(5882), 1444-1449. <https://doi.org/10.1126/science.1155121>.
6. Cai, W., Li, K., Liao, H., Wang, H., & Wu, L. (2017). Weather conditions conducive to Beijing severe haze more frequent under climate change. *Nature Climate Change*, 7(4), 257-262. <https://doi.org/10.1038/nclimate3249>.
7. Collins, M., Chandler, R. E., Cox, P. M., Huthnance, J. M., Rougier, J., & Stephenson, D. B. (2012). Quantifying future climate change. *Nature Climate Change*, 2(6), 403-409. <https://doi.org/10.1038/nclimate1414>.
8. Collins, W. J., et al. (2011). Development and evaluation of an Earth-System model – HadGEM2. *Geoscientific Model Development*, 4(4), 1051-1075. <https://doi.org/10.5194/gmd-4-1051-2011>.
9. Cramer, W., et al. (2001). Global response of terrestrial ecosystem structure and function to CO₂ and climate change: results from six dynamic global vegetation models. *Global Change Biology*, 7(4), 357-373. <https://doi.org/10.1046/j.1365-2486.2001.00383.x>.
10. Dan, L., Cao, F., & Gao, R. (2015). The improvement of a regional climate model by coupling a land surface model with eco-physiological processes: A case study in 1998. *Climatic Change*, 129(3-4), 457-470. <https://doi.org/10.1007/s10584-013-0997-8>.
11. Dee, D. P., Uppala, S., Simmons, A., Berrisford, P., Poli, P., Kobayashi, S., Andrae, U., Balsameda, M., Balsamo, G., & Bauer, P. (2011). The ERA-Interim reanalysis: Configuration and performance of the data assimilation system. *Quarterly Journal of the Royal Meteorological Society*, 137(656), 553-597. <https://doi.org/10.1002/qj.828>.
12. Diffenbaugh, N. S., & Field, C. B. (2013). Changes in ecologically critical terrestrial climate conditions. *Science*, 341(6145), 486-492. <https://doi.org/10.1126/science.1237123>.
13. Emanuel, K. A. (1991). A Scheme for Representing Cumulus Convection in Large-Scale Models. *Journal of the Atmospheric Sciences*, 48(21), 2313-2329. [https://doi.org/10.1175/1520-0469\(1991\)048<2313:Asfrcc>2.0.Co;2](https://doi.org/10.1175/1520-0469(1991)048<2313:Asfrcc>2.0.Co;2).

14. Erfanian, A., Wang, G., Yu, M., & Anyah, R. (2016). Multimodel ensemble simulations of present and future climates over West Africa: Impacts of vegetation dynamics. *Journal of Advances in Modeling Earth Systems*, 8(3), 1411-1431. <https://doi.org/10.1002/2016MS000660>.
15. Erfanian, A., Wang, G. L., Fomenko, L., & Yu, M. (2017). Ensemble-based Reconstructed Forcing (ERF) for regional climate modeling: Attaining the performance at a fraction of cost. *Geophysical Research Letters*, 44(7), 3290-3298. <https://doi.org/10.1002/2017gl073053>.
16. Gang, C. C., Zhang, Y. Z., Wang, Z. Q., Chen, Y. Z., Yang, Y., Li, J. L., Cheng, J. M., Qi, J. G., & Odeh, I. (2017). Modeling the dynamics of distribution, extent, and NPP of global terrestrial ecosystems in response to future climate change. *Global and Planetary Change*, 148, 153-165. <https://doi.org/10.1016/j.gloplacha.2016.12.007>.
17. Gao, J., Jiao, K., Wu, S., Ma, D., Zhao, D., Yin, Y., & Dai, E. (2017). Past and future effects of climate change on spatially heterogeneous vegetation activity in China. *Earth's Future*, 5(7), 679-692. <https://doi.org/10.1002/2017ef000573>.
18. Gao, X., Shi, Y., Han, Z., Wang, M., Wu, J., Zhang, D., Xu, Y., & Giorgi, F. (2017). Performance of RegCM4 over major river basins in China. *Advances in Atmospheric Sciences*, 34(4), 441-455. <https://doi.org/10.1007/s00376-016-6179-7>.
19. Gao, X.-J., Wu, J., Shi, Y., Wu, J., Han, Z.-Y., Zhang, D.-F., Tong, Y., Li, R.-K., Xu, Y., & Giorgi, F. (2018). Future changes in thermal comfort conditions over China based on multi-RegCM4 simulations. *Atmospheric and Oceanic Science Letters*, 11(4), 291-299. <https://doi.org/10.1080/16742834.2018.1471578>
20. Gao, X., Xu, Y., Zhao, Z., Pal, J. S., & Giorgi, F. (2006). On the role of resolution and topography in the simulation of East Asia precipitation. *Theoretical and Applied Climatology*, 86(1-4), 173-185. <https://doi.org/10.1007/s00704-005-0214-4>.
21. Gent, P. R., et al. (2011). The Community Climate System Model Version 4. *Journal of Climate*, 24(19), 4973-4991. <https://doi.org/10.1175/2011jcli4083.1>.
22. Giorgi, F., et al. (2012). RegCM4: model description and preliminary tests over multiple CORDEX domains. *Climate Research*, 52, 7-29. <https://doi.org/10.3354/cr01018>.
23. Griffies, S. M., et al. (2011). The GFDL CM3 Coupled Climate Model: Characteristics of the Ocean and Sea Ice Simulations. *Journal of Climate*, 24(13), 3520-3544. <https://doi.org/10.1175/2011jcli3964.1>.
24. Hall, A. (2014). Climate. Projecting regional change. *Science*, 346(6216), 1461-1462. <https://doi.org/10.1126/science.aaa0629>.
25. Harris, I., Jones, P. D., Osborn, T. J., & Lister, D. H. (2014). Updated high-resolution grids of monthly climatic observations - the CRU TS3.10 Dataset. *International Journal of Climatology*, 34(3), 623-642. <https://doi.org/10.1002/joc.3711>.
26. He, C., & Zhou, T. (2015). Responses of the Western North Pacific Subtropical High to Global Warming under RCP4.5 and RCP8.5 Scenarios Projected by 33 CMIP5 Models: The Dominance of Tropical Indian Ocean–Tropical Western Pacific SST Gradient. *Journal of Climate*, 28(1), 365-380. <https://doi.org/10.1175/jcli-d-13-00494.1>.
27. Holtslag, A. A. M., De Bruijn, E. I. F., & Pan, H. L. (1990). A High Resolution Air Mass Transformation Model for Short-Range Weather Forecasting. *Monthly Weather Review*, 118(8), 1561-1575. [https://doi.org/10.1175/1520-0493\(1990\)118<1561:Ahramt>2.0.Co;2](https://doi.org/10.1175/1520-0493(1990)118<1561:Ahramt>2.0.Co;2).
28. Jiang, D., & Tian, Z. (2012). East Asian monsoon change for the 21st century: Results of CMIP3 and CMIP5 models. *Chinese Science Bulletin*, 58(12), 1427-1435. <https://doi.org/10.1007/s11434-012-5533-0>.
29. Kawase, H., Yoshikane, T., Hara, M., Kimura, F., Yasunari, T., Ailikun, B., Ueda, H., & Inoue, T. (2009). Intermodel variability of future changes in the Baiu rainband estimated

- by the pseudo global warming downscaling method. *Journal of Geophysical Research*, 114(D24). <https://doi.org/10.1029/2009jd011803>.
30. Kiehl, J. T., Hack, J. J., Bonan, G. B., Boville, B. A., Briegleb, B. P., Williamson, D. L., & Rasch, P. J. (1996), Description of the NCAR Community Climate Model (CCM3). *NCAR Tech. Note NCAR/TN-420ISTR*, 152 pp., Natl. Cent. for Atmos. Res., Boulder, Colo.
 31. Lawrence, D. M., et al. (2011). Parameterization Improvements and Functional and Structural Advances in Version 4 of the Community Land Model. *Journal of Advances in Modeling Earth Systems*, 3(3). <https://doi.org/10.1029/2011MS00045>.
 32. Lawrence, P. J., & Chase, T. N. (2007). Representing a new MODIS consistent land surface in the Community Land Model (CLM 3.0). *Journal of Geophysical Research*, 112(G1), 252-257. <https://doi.org/10.1029/2006jg000168>.
 33. Lee, X., Goulden, M. L., Hollinger, D. Y., Barr, A., Black, T. A., Bohrer, G., Bracho, R., Drake, B., Goldstein, A., & Gu, L. (2011). Observed increase in local cooling effect of deforestation at higher latitudes. *Nature*, 479(7373), 384. <https://doi.org/nature10588>.
 34. Li, L., et al. (2013). The flexible global ocean-atmosphere-land system model, Grid-point Version 2: FGOALS-g2. *Advances in Atmospheric Sciences*, 30(3), 543-560. <https://doi.org/10.1007/s00376-012-2140-6>.
 35. Li, Z., Sun, Y., Li, T., Ding, Y., & Hu, T. (2019). Future Changes in East Asian Summer Monsoon Circulation and Precipitation Under 1.5 to 5 °C of Warming. *Earth's Future*, 7(12), 1391-1406. <https://doi.org/10.1029/2019ef001276>
 36. Liu, Y., Xue, Y., MacDonald, G., Cox, P., & Zhang, Z. (2019). Global vegetation variability and its response to elevated CO₂, global warming, and climate variability – a study using the offline SSiB4/TRIFFID model and satellite data. *Earth System Dynamics*, 10(1), 9-29. <https://doi.org/10.5194/esd-10-9-2019>.
 37. Ma, D., Notaro, M., Liu, Z., Chen, G., & Liu, Y. (2013). Simulated impacts of afforestation in East China monsoon region as modulated by ocean variability. *Climate Dynamics*, 41(9-10), 2439-2450. <https://doi.org/10.1007/s00382-012-1592-9>.
 38. Mearns, L. O., et al. (2012). The North American Regional Climate Change Assessment Program: Overview of Phase I Results. *Bulletin of the American Meteorological Society*, 93(9), 1337-1362. <https://doi.org/10.1175/bams-d-11-00223.1>
 39. Murray-Tortarolo, G., et al. (2013). Evaluation of Land Surface Models in Reproducing Satellite-Derived LAI over the High-Latitude Northern Hemisphere. Part I: Uncoupled DGVMs. *Remote Sensing*, 5(10), 4819-4838. <https://doi.org/10.3390/rs5104819>.
 40. Moss, R. H., et al. (2010). The next generation of scenarios for climate change research and assessment. *Nature*, 463(7282), 747-756. <https://doi.org/10.1038/nature08823>.
 41. Nemani, R. R., Keeling, C. D., Hashimoto, H., Jolly, W. M., Piper, S. C., Tucker, C. J., Myneni, R. B., & Running, S. W. (2003). Climate-driven increases in global terrestrial net primary production from 1982 to 1999. *Science*, 300(5625), 1560-1563. <https://doi.org/10.1126/science.1082750>.
 42. Niu, X., Tang, J., Wang, S., & Fu, C. (2018). Impact of future land use and land cover change on temperature projections over East Asia. *Climate Dynamics*, 52(11), 6475-6490. <https://doi.org/10.1007/s00382-018-4525-4>.
 43. Notaro, M., Chen, G., & Liu, Z. (2011). Vegetation Feedbacks to Climate in the Global Monsoon Regions*. *Journal of Climate*, 24(22), 5740-5756. <https://doi.org/10.1175/2011jcli4237.1>.
 44. Notaro, M., Chen, G., Yu, Y., Wang, F., & Tawfik, A. (2017). Regional Climate Modeling of Vegetation Feedbacks on the Asian–Australian Monsoon Systems. *Journal of Climate*, 30(5), 1553-1582. <https://doi.org/10.1175/JCLI-D-16-0669.1>.

45. Oleson, K., Lawrence, D., Gordon, B., Flanner, M., Kluzek, E., Peter, J., Levis, S., Swenson, S., Thornton, P., & Feddema, J. (2013), Technical description of version 4.5 of the Community Land Model (CLM), *NCAR Tech. Note NCAR/TN-5031STR*, 420 pp., Natl. Cent. for Atmos. Res., Boulder, Colo., doi:10.5065/D6RR1W7M.
46. Oleson, K. W., Lawrence, D. M., Gordon, B., Flanner, M. G., Kluzek, E., Peter, J., Levis, S., Swenson, S. C., Thornton, E., & Feddema, J. (2010), Technical description of version 4.0 of the Community Land Model (CLM)., *NCAR Technical Note NCAR/TN-478+STR*, Natl. Cent. for Atmos. Res., Boulder, Colo.
47. Schaller, N., Mahlstein, I., Cermak, J., & Knutti, R. (2011). Analyzing precipitation projections: A comparison of different approaches to climate model evaluation. *Journal of Geophysical Research*, 116(D10). <https://doi.org/10.1029/2010jd014963>.
48. Shi, Y., Wang, G., & Gao, X. (2017). Role of resolution in regional climate change projections over China. *Climate Dynamics*, 51(5-6), 2375-2396. <https://doi.org/10.1007/s00382-017-4018-x>.
49. Shi, Y., Yu, M., Erfanian, A., & Wang, G. (2018). Modeling the Dynamic Vegetation–Climate System over China Using a Coupled Regional Model. *Journal of Climate*, 31(15), 6027-6049. <https://doi.org/10.1175/jcli-d-17-0191.1>.
50. Sitch, S., et al. (2008). Evaluation of the terrestrial carbon cycle, future plant geography and climate-carbon cycle feedbacks using five Dynamic Global Vegetation Models (DGVMs). *Global Change Biology*, 14(9), 2015-2039. <https://doi.org/10.1111/j.1365-2486.2008.01626.x>.
51. Swann, A. L., Hoffman, F. M., Koven, C. D., & Randerson, J. T. (2016). Plant responses to increasing CO₂ reduce estimates of climate impacts on drought severity. *Proceedings of the National Academy of Sciences*, 113(36), 10019-10024. <https://doi.org/10.1073/pnas.1604581113>.
52. Wakazuki, Y., & Rasmussen, R. (2015). Incremental dynamical downscaling for probabilistic analysis based on multiple GCM projections. *Geophysical Research Letters*, 42(24), 10847-10855. <https://doi.org/10.1002/2015gl066242>.
53. Wang, G., Yu, M., Pal, J. S., Mei, R., Bonan, G. B., Levis, S., & Thornton, P. E. (2016). On the development of a coupled regional climate–vegetation model RCM–CLM–CN–DV and its validation in Tropical Africa. *Climate Dynamics*, 46(1-2), 515-539. <https://doi.org/10.1007/s00382-015-2596-z>.
54. Wei, J., Jin, Q., Yang, Z.-L., & Zhou, L. (2017). Land-atmosphere-aerosol coupling in North China during 2000-2013. *International Journal of Climatology*, 37, 1297-1306. <https://doi.org/10.1002/joc.4993>.
55. White, R. H., & Toumi, R. (2013). The limitations of bias correcting regional climate model inputs. *Geophysical Research Letters*, 40(12), 2907-2912. <https://doi.org/10.1002/grl.50612>.
56. Wu, J., & Gao, X. J. (2013). A gridded daily observation dataset over China region and comparison with the other datasets. *Chinese Journal of Geophysics*, 56, 1102–1111. (in Chinese). <https://doi.org/10.6038/cjg20130406>
57. Wu, J., Han, Z., Xu, Y., Zhou, B., & Gao, X. (2020). Changes in Extreme Climate Events in China Under 1.5 °C–4 °C Global Warming Targets: Projections Using an Ensemble of Regional Climate Model Simulations. *Journal of Geophysical Research: Atmospheres*, 125(2). <https://doi.org/10.1029/2019jd031057>
58. Xie, S.-P., et al. (2015). Towards predictive understanding of regional climate change. *Nature Climate Change*, 5(10), 921-930. <https://doi.org/10.1038/nclimate2689>.
59. Xu, Z., Han, Y., & Yang, Z. (2018). Dynamical downscaling of regional climate: A review of methods and limitations. *Science China Earth Sciences*, 62(2), 365-375. <https://doi.org/10.1007/s11430-018-9261-5>.

60. Xue, Y., De Sales, F., Vasic, R., Mechoso, C. R., Arakawa, A., & Prince, S. (2010). Global and seasonal assessment of interactions between climate and vegetation biophysical processes: a GCM study with different land–vegetation representations. *Journal of Climate*, 23(6), 1411-1433. <https://doi.org/10.1175/2009JCLI3054.1>.
61. Yu, D., Liu, Y., Shi, P., & Wu, J. (2019). Projecting impacts of climate change on global terrestrial ecoregions. *Ecological Indicators*, 103, 114-123. <https://doi.org/10.1016/j.ecolind.2019.04.006>.
62. Yu, E., Wang, H., Sun, J., & Gao, Y. (2013). Climatic response to changes in vegetation in the Northwest Hetao Plain as simulated by the WRF model. *International Journal of Climatology*, 33(6), 1470-1481. <https://doi.org/10.1002/joc.3527>.
63. Yu, M., Wang, G., Parr, D., & Ahmed, K. F. (2014). Future changes of the terrestrial ecosystem based on a dynamic vegetation model driven with RCP8.5 climate projections from 19 GCMs. *Climatic Change*, 127(2), 257-271. <https://doi.org/10.1007/s10584-014-1249-2>.
64. Yu, M., Wang, G., & Pal, J. S. (2016). Effects of vegetation feedback on future climate change over West Africa. *Climate Dynamics*, 46(11-12), 1-20. <https://doi.org/10.1007/s00382-015-2795-7>.
65. Zhou, C., Chen, D., Wang, K., Dai, A., & Qi, D. (2020). Conditional Attribution of the 2018 Summer Extreme Heat over Northeast China: Roles of Urbanization, Global Warming, and Warming-Induced Circulation Changes. *Bulletin of the American Meteorological Society*, 101(1), S71-S76. <https://doi.org/10.1175/bams-d-19-0197.1>
66. Zhu, Z., et al. (2016). Greening of the Earth and its drivers. *Nature Climate Change*, 6(8), 791-795. <https://doi.org/10.1038/nclimate3004>.

Table 1. Reanalysis and CMIP5 coupled models used in this study. A single realization, as specified, is employed for each model.

Model name	Model center	Realization	Atmosphere resolution (lat x lon)	Calendar	References
ERA-Interim	ECWMF	/	241 x 480	gregorian	(Dee et al., 2011)
CCSM4	NCAR	r6i1p1	192 x 288	noleap	(Gent et al., 2011)
FGOALS-g2	LASG-CESS	r1i1p1	60 x 128	noleap	(Li et al., 2013)
GFDL-CM3	GFDL	r1i1p1	90 x 144	noleap	(Griffies et al., 2011)
HadGEM2-ES	MOHC	r1i1p1	144 x 192	360-day	(Collins et al., 2011)

Table 2. Mean and standard deviation of 2-m surface air temperature (in °C) and precipitation (in mm day⁻¹) spatially averaged over East Asia Summer Monsoon region, from two observational datasets and the RCM-CLM-CNDV experiments as well as the projected future changes (RCP8.5 – Historical).

Observation/ model	2-m air surface temperature (°C)			Precipitation (mm day ⁻¹)		
	historical	RCP8.5	Changes	historical	RCP8.5	Changes
CRU	24.63 ± 0.52			5.12 ± 1.31		
CN05.1	24.07 ± 0.61			5.27 ± 1.50		
ERA (PGW)	24.26 ± 0.65	29.71 ± 0.69	5.45	5.83 ± 1.48	6.34 ± 1.76	0.51
MME	23.73 ± 0.38	28.96 ± 0.42	5.23	4.89 ± 0.70	6.00 ± 0.78	1.11
CCSM4	24.63 ± 0.69	29.18 ± 0.91	4.55	5.20 ± 1.32	5.72 ± 1.57	0.52
FGOALS-g2	23.48 ± 0.72	27.13 ± 0.71	3.65	5.49 ± 1.41	6.90 ± 1.62	1.41
GFDL-CM3	22.99 ± 1.01	30.37 ± 0.91	7.38	3.68 ± 1.18	4.65 ± 1.42	0.97
HadGEM2-ES	23.83 ± 0.59	29.14 ± 0.56	5.31	5.20 ± 1.15	6.74 ± 1.74	1.54

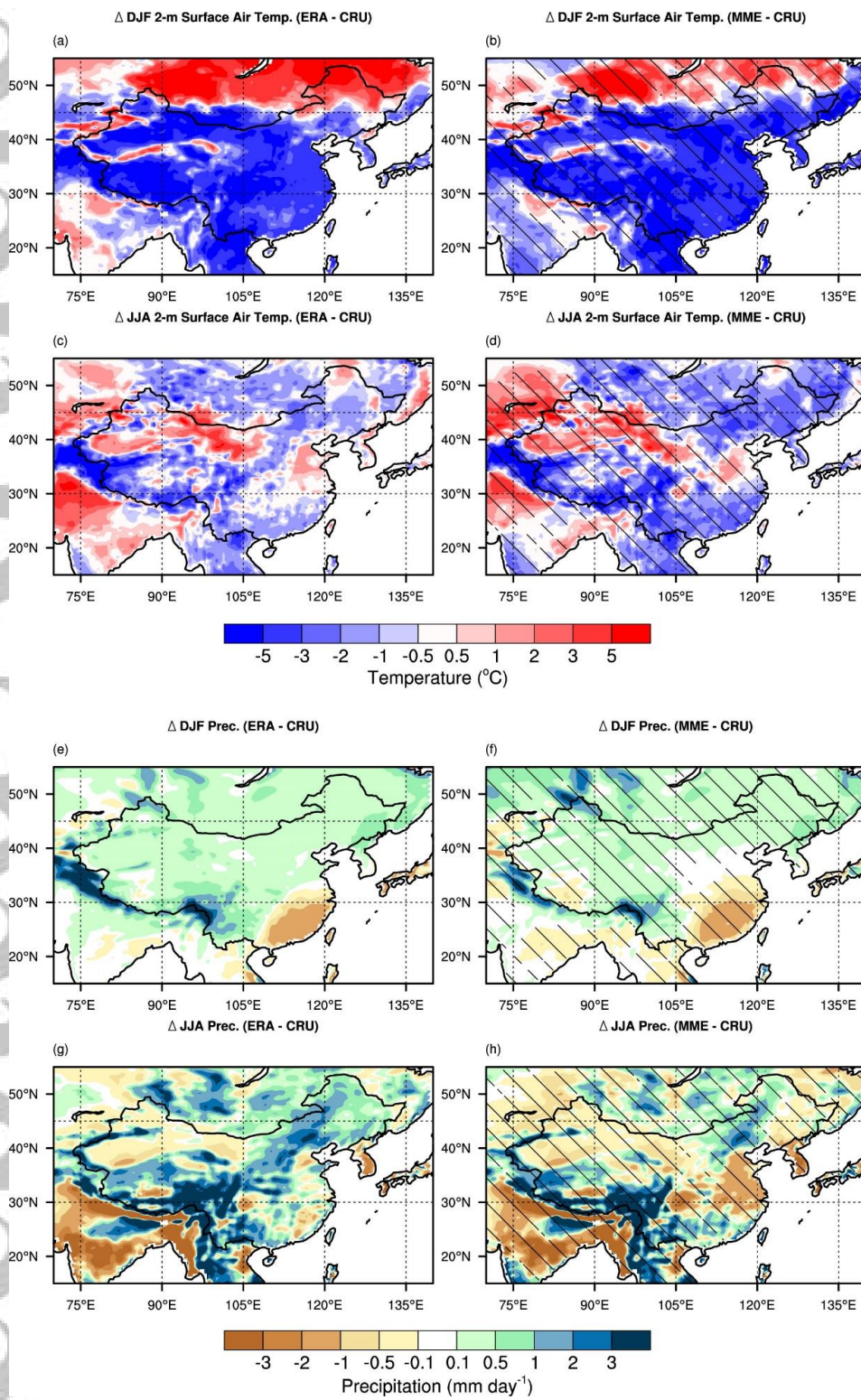


Figure 1. Model biases of 2-m surface air temperature (a-d, units: °C) and precipitation (e-h, units: mm day⁻¹) from RCM-CLM-CNDV experiments compared to CRU observation during the 1980-1999 period. The oblique lines indicate areas where 3 to 4 members agree with the MME results on the sign of the model biases.

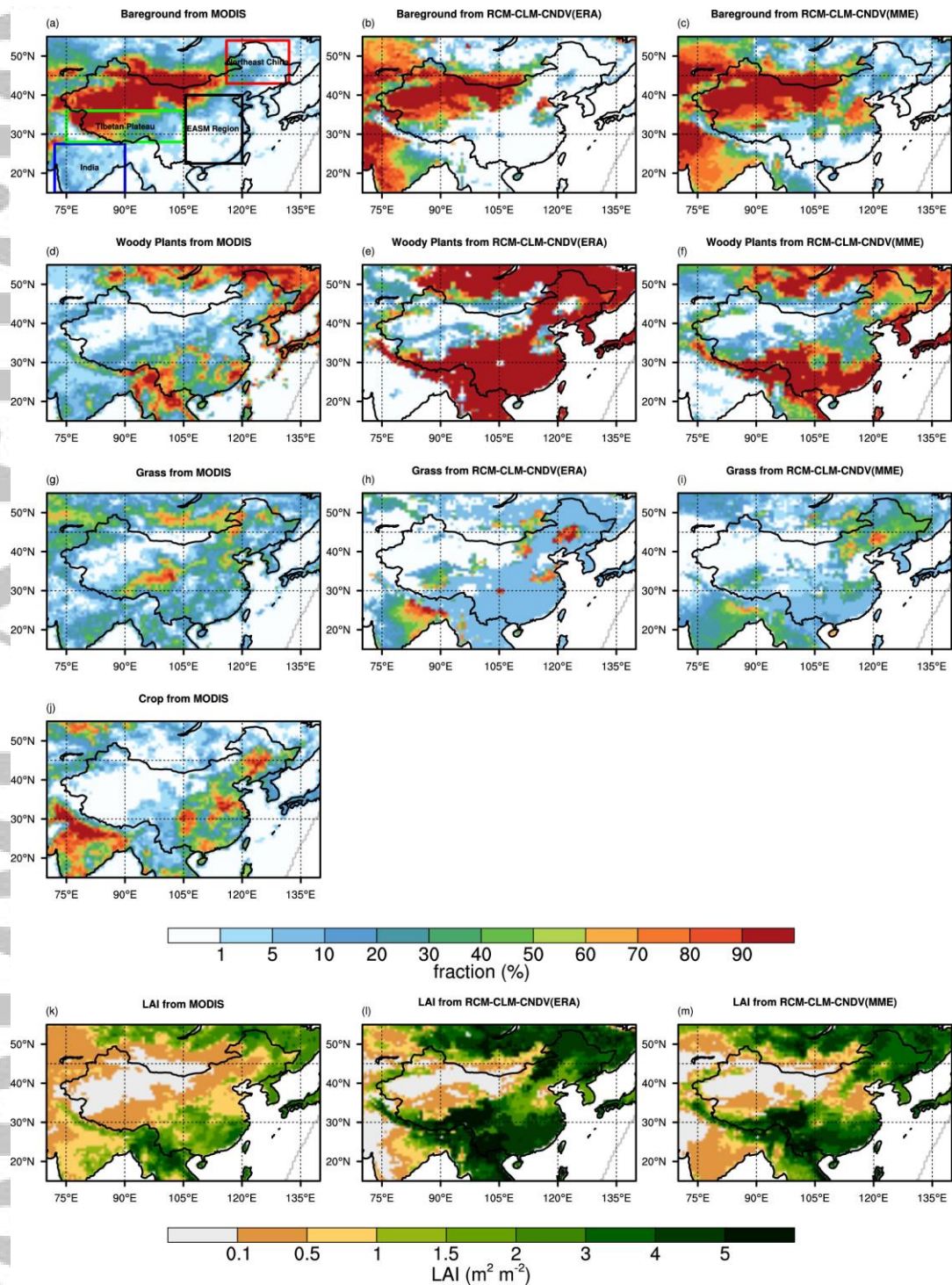


Figure 2. Coverage (in %) for bare ground (a-c), woody plants (d-f), grasses (g-i) and crops (j) and the grid-average of leaf area index (k-m, units: m^2/m^2): from satellite data used to prescribe vegetation in RCM-CLM (a, d, g, j, k) and from the RCM-CLM-CNDV present-day simulation forced by ERA (b, e, h, l) and GCM-driven MME results (c, f, i, m). The red, green, blue and black rectangles in Panel (a) mark the regions used for spatial averaging over Northeast China, Tibetan Plateau, India and East Asian Summer Monsoon region, respectively.

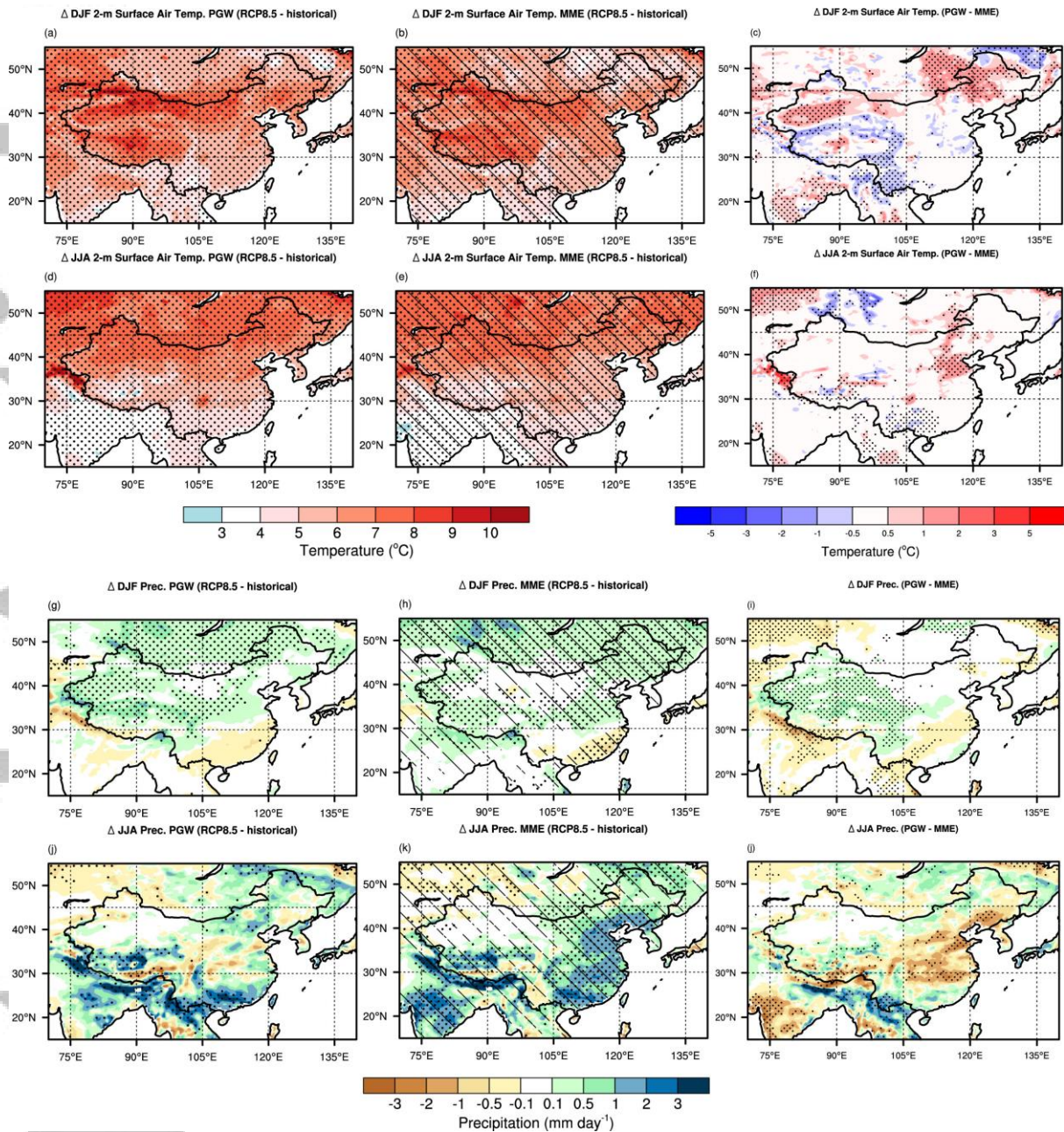


Figure 3. Changes in the spatial distribution of 2-m air surface temperature (a-f) and precipitation (g-l) between the historical and the RCP8.5 experiments as simulated by the RCM-CLM-CNDV using the PGW (a, d, g, j), the MME approach (b, e, h, k) and the differences between PGW and MME (c, f, i, l). The oblique lines indicate the areas where 3 to 4 members agree with the MME results on the sign of projected future changes. Black dots indicate areas where the changes or differences pass the 5% significance test.

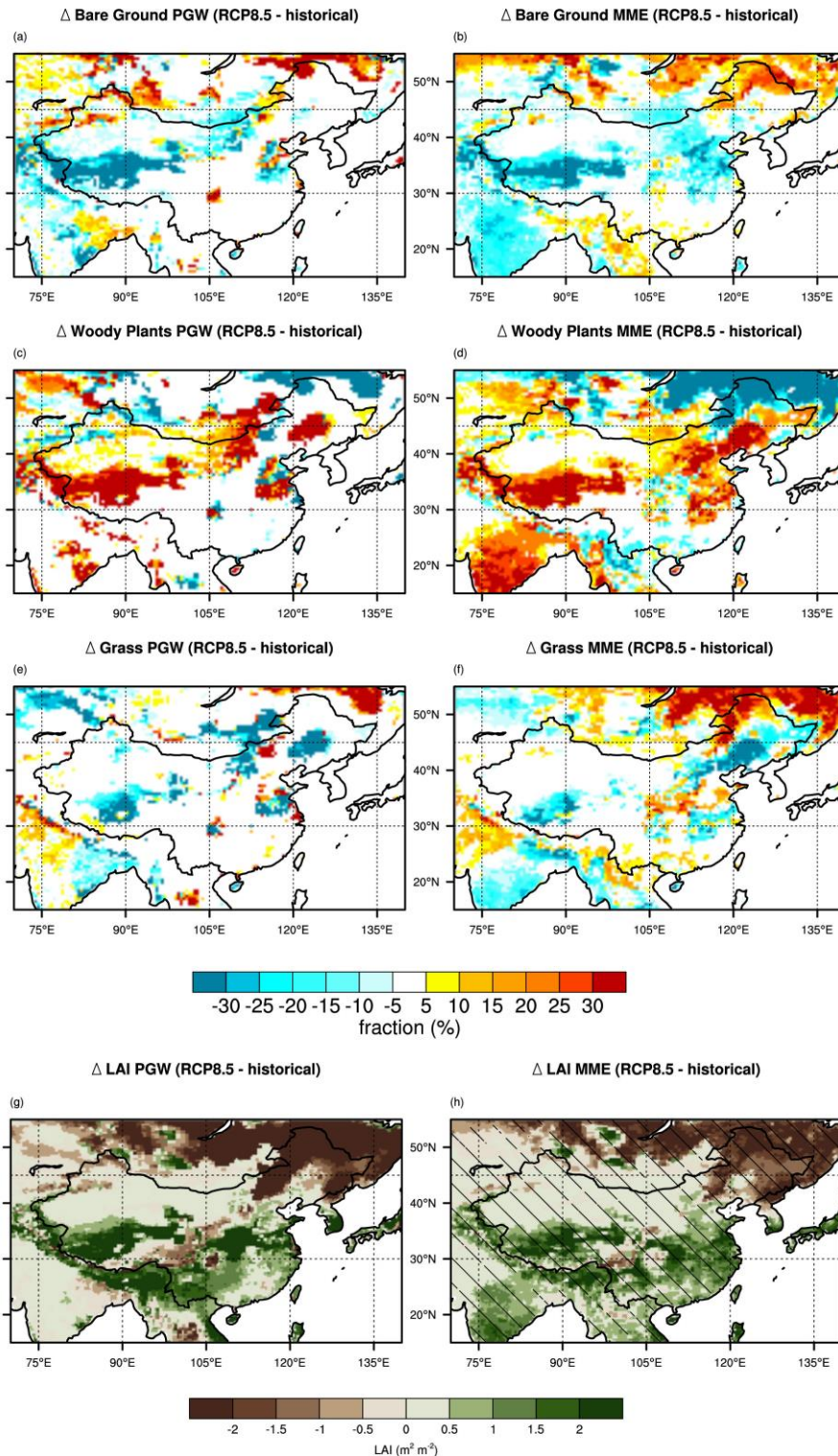


Figure 4. Projected future changes in bare ground (1st row), woody plants (2nd row), grasses (3rd row) cover (in %) and LAI (4th row; in m² m⁻²), based on PGW (left column) and MME (right column) approaches. The oblique lines indicate areas where 3 to 4 members agree with the MME results on the direction of future changes.

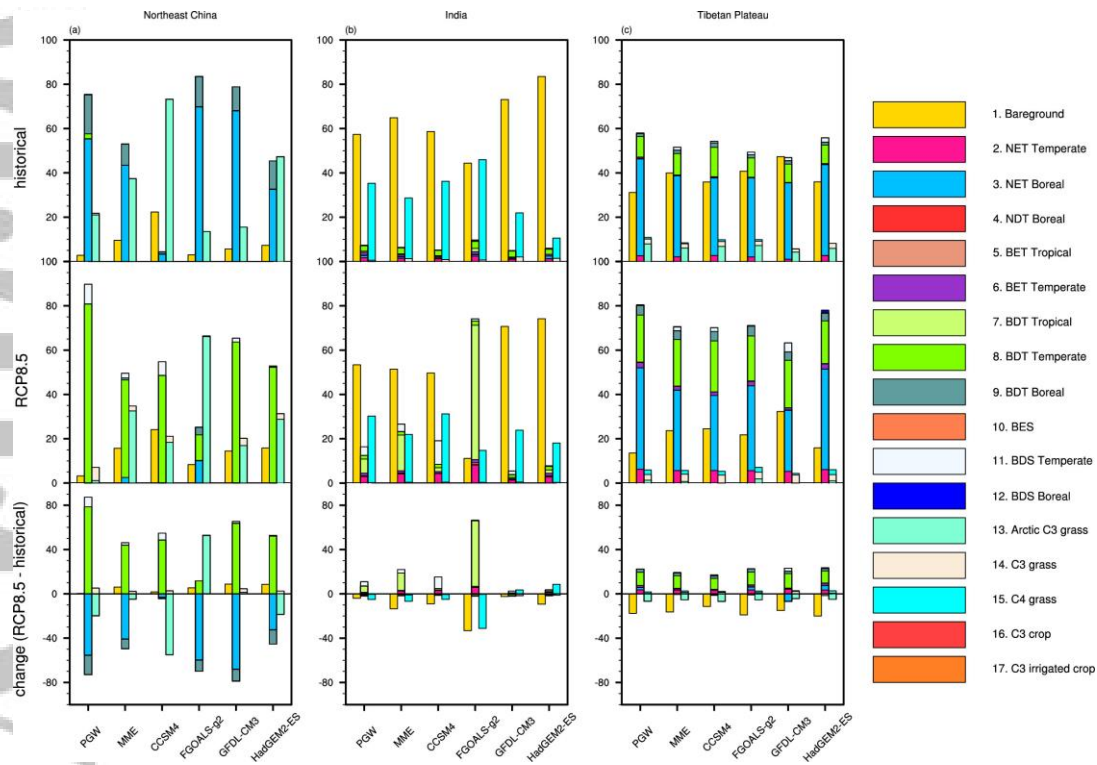


Figure 5. Historical simulations, RCP8.5 projections, and projected future changes of bare ground, woody plants and grass coverage (superimposed bars from top to bottom) spatially averaged over (a) Northeast China, (b) India and (c) Tibetan Plateau. The segments in each bar represent up to 17 different PFTs: 1. Bare ground; 2. Needleleaf evergreen temperate tree; 3. Needleleaf evergreen boreal tree; 4. Needleleaf deciduous boreal tree; 5. Broadleaf evergreen tropical tree; 6. Broadleaf evergreen temperate tree; 7. Broadleaf deciduous tropical tree; 8. Broadleaf deciduous temperate tree; 9. Broadleaf deciduous boreal tree; 10. Broadleaf evergreen shrub; 11. Broadleaf deciduous temperate shrub; 12. Broadleaf deciduous boreal shrub; 13. Arctic C3 grass; 14. C3 grass; 15. C4 grass; 16. C3 crop; 17. C3 irrigated crop.

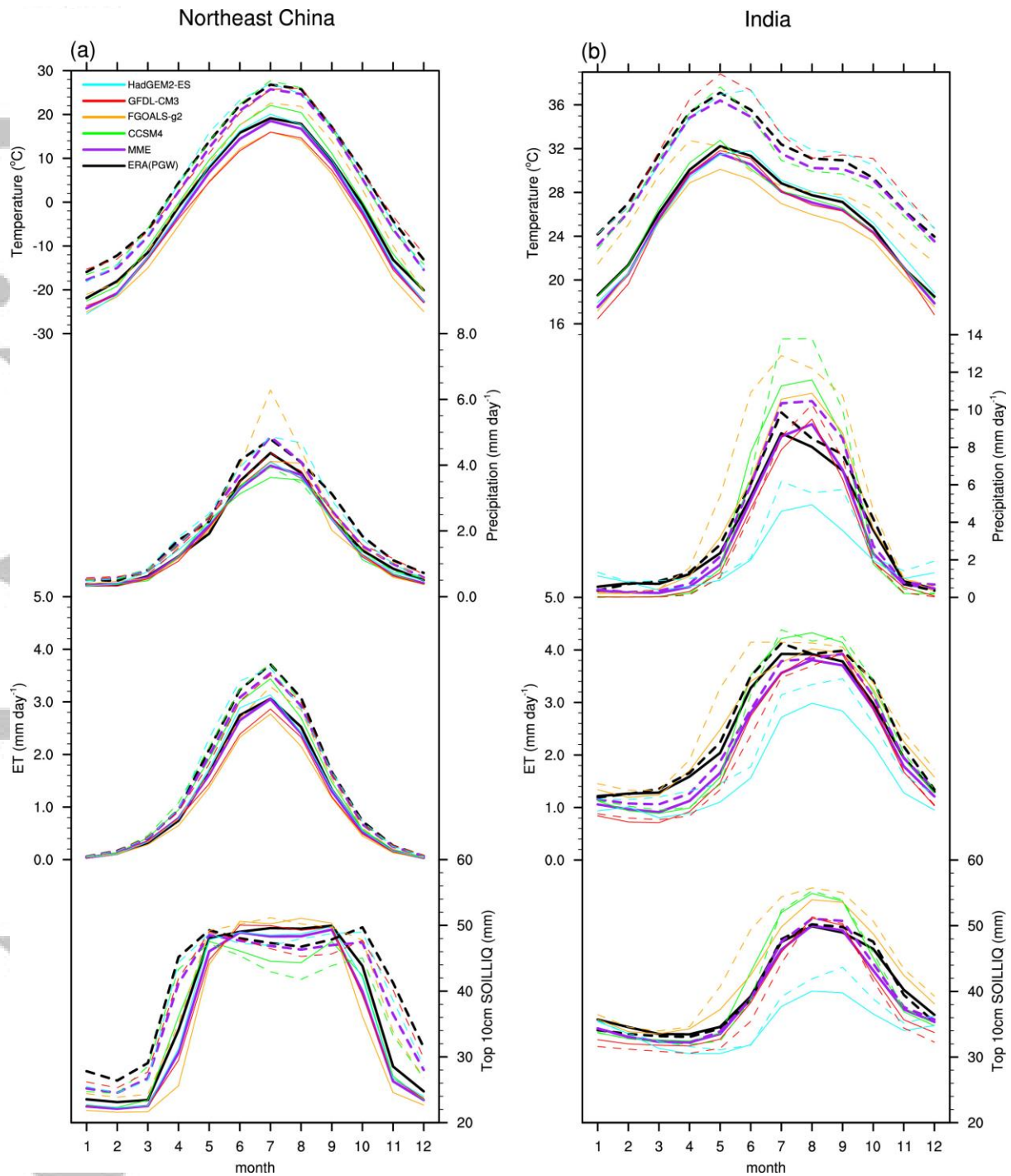


Figure 6. Seasonal cycle of 2-m air surface temperature (units: °C), precipitation (units: mm day⁻¹), ET (mm day⁻¹) and moisture content in the top 10 cm soil (units: mm) spatially averaged over Northeast China region (a) and India (b). Solid and dash lines for historical and RCP8.5, respectively.

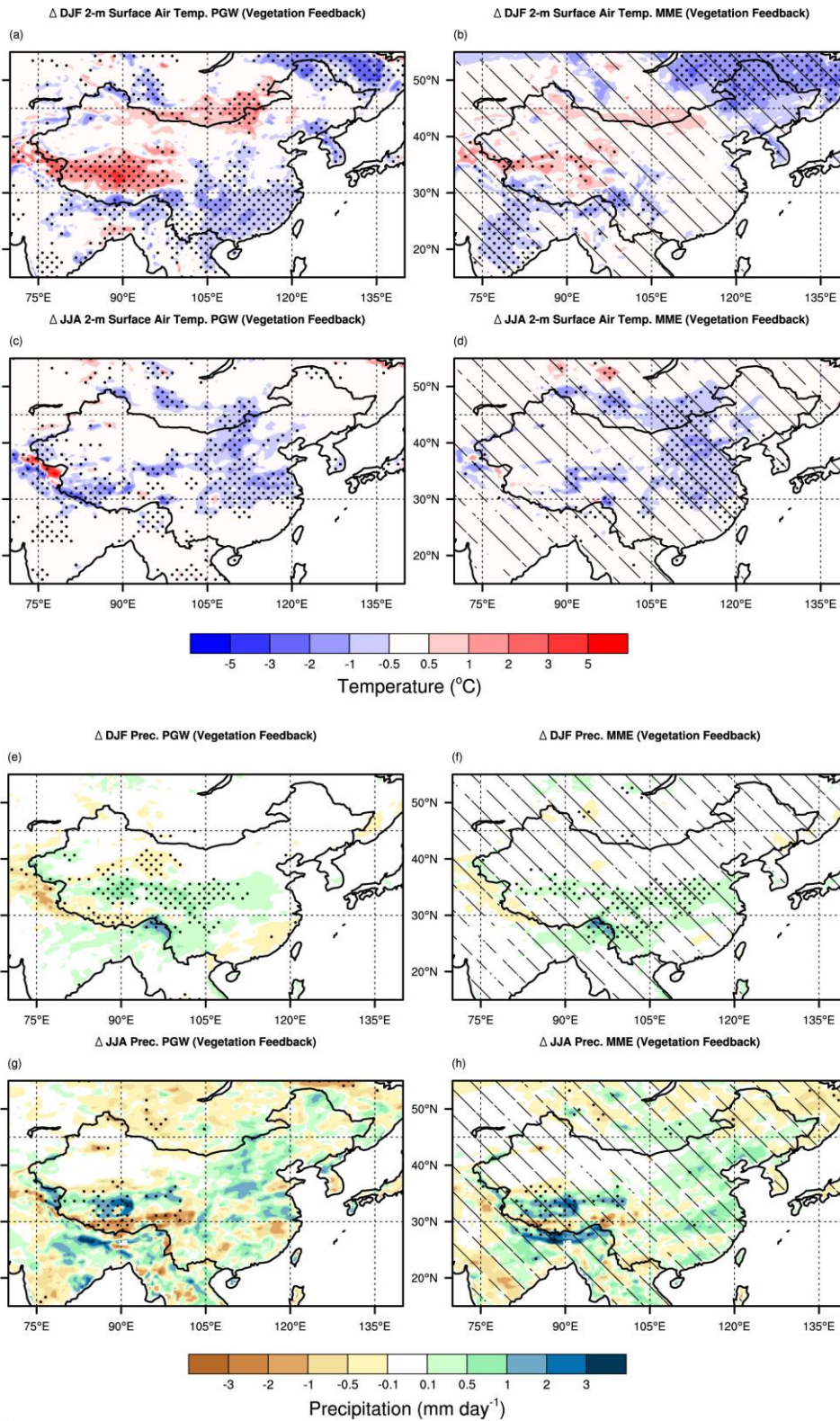


Figure 7. Impacts of dynamic vegetation feedback on projected changes of temperature (a-d, units: °C) and precipitation (e-h, units: mm day⁻¹), from PGW (a, c, e, g) and MME (b, d, f, h). The oblique lines indicate areas where 3 to 4 members agree with the MME results, and black dots indicate areas where the changes or differences pass the 5% significance test.

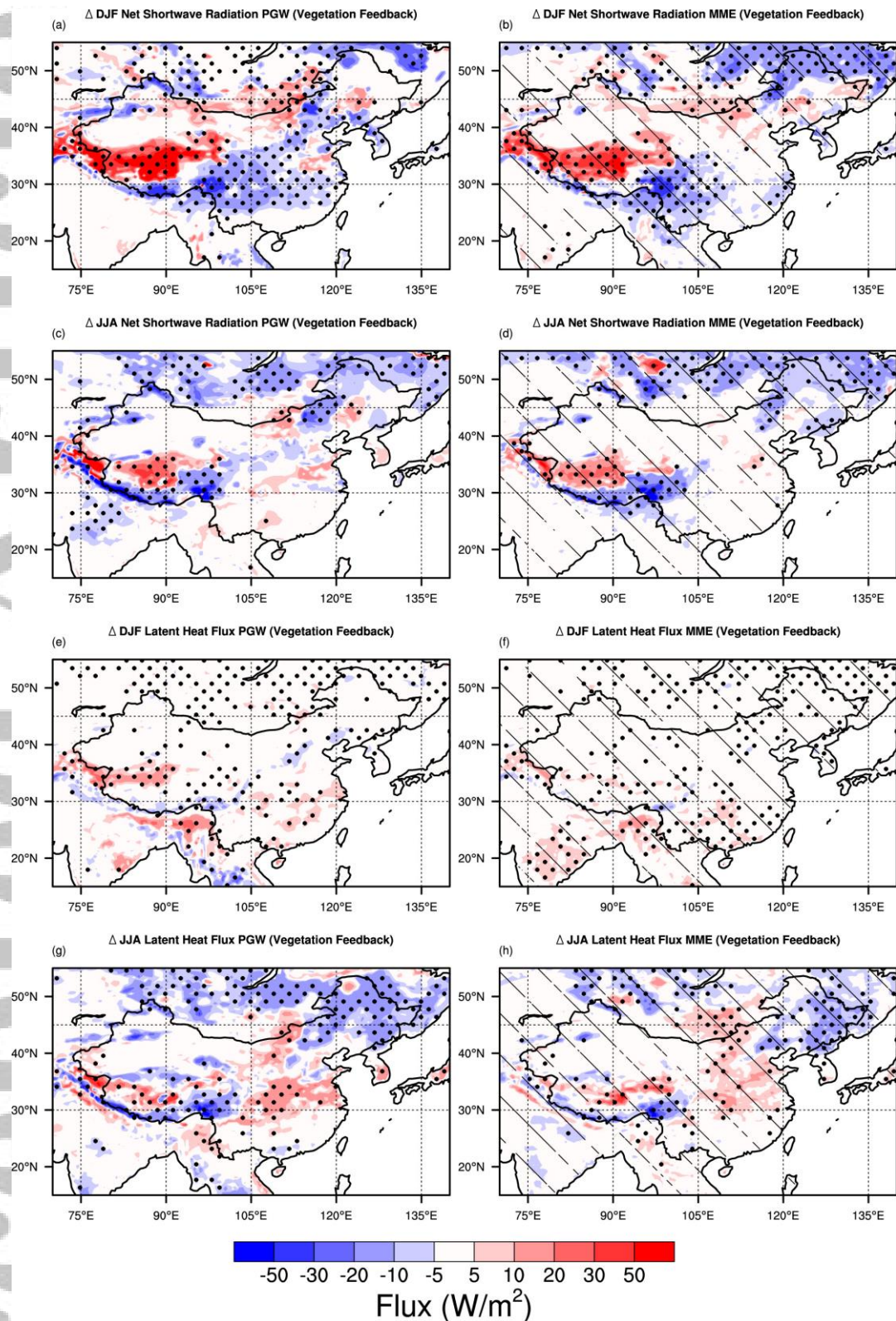


Figure 8. Impacts of dynamic vegetation feedback on changes of net shortwave radiation (a-d) and latent heat flux (e-h) (units: $W m^{-2}$) from PGW (a, c, e, g) and MME (b, d, f, h) in DJF (a, b, e, f) and JJA (c, d, g, h). The oblique lines indicate areas where 3 to 4 members agree with the MME results, and black dots indicate areas where the changes or differences pass the 5% significance test.

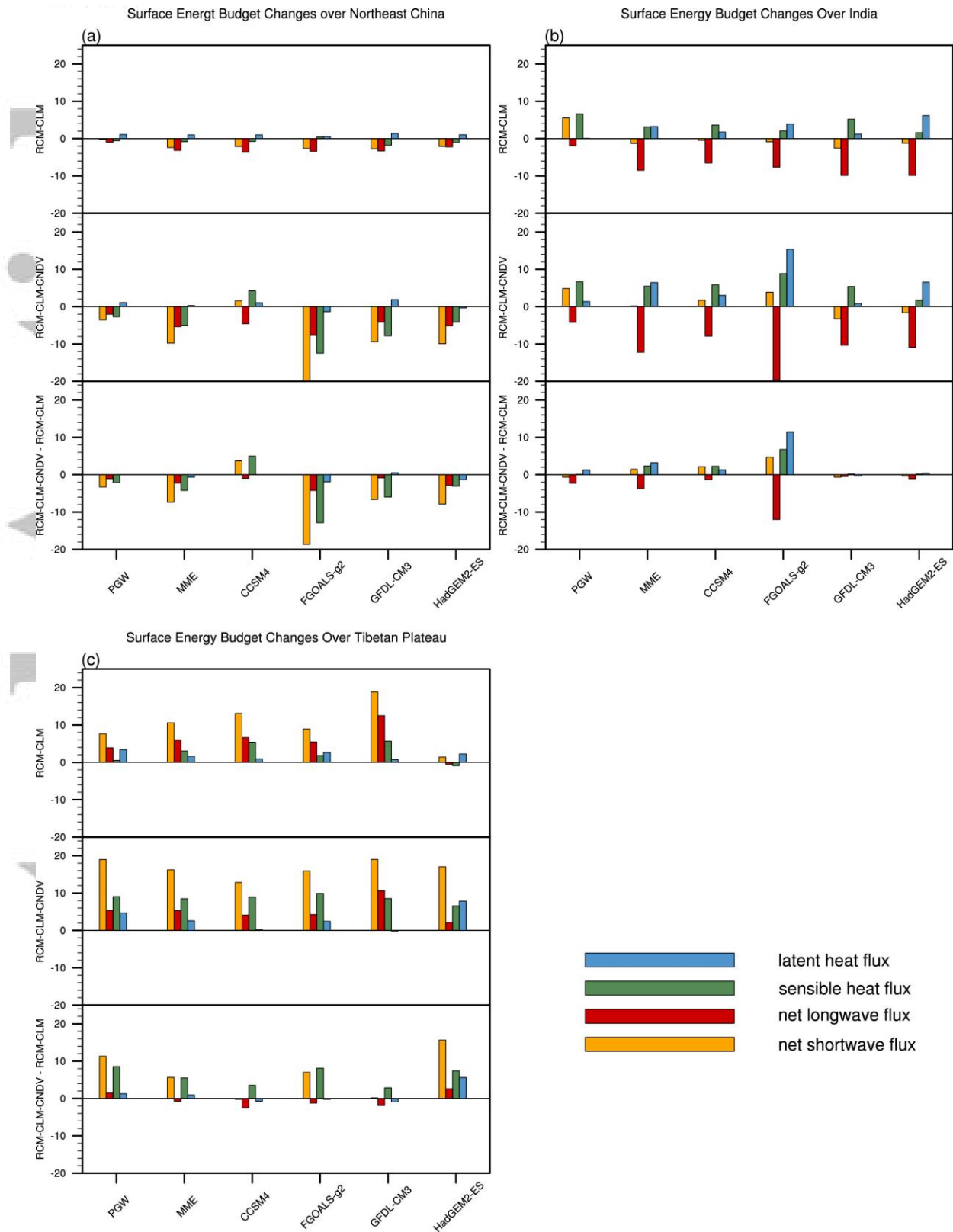


Figure 9. Dynamic vegetation feedback on future changes of net shortwave radiation, net longwave radiation, sensible heat flux and latent heat flux changes (units: $W m^{-2}$), spatially averaged over Northeast China (a), India (b) and Tibetan Plateau(c) regions. The impacts of vegetation feedback on ground heat flux is negligible and not included here.

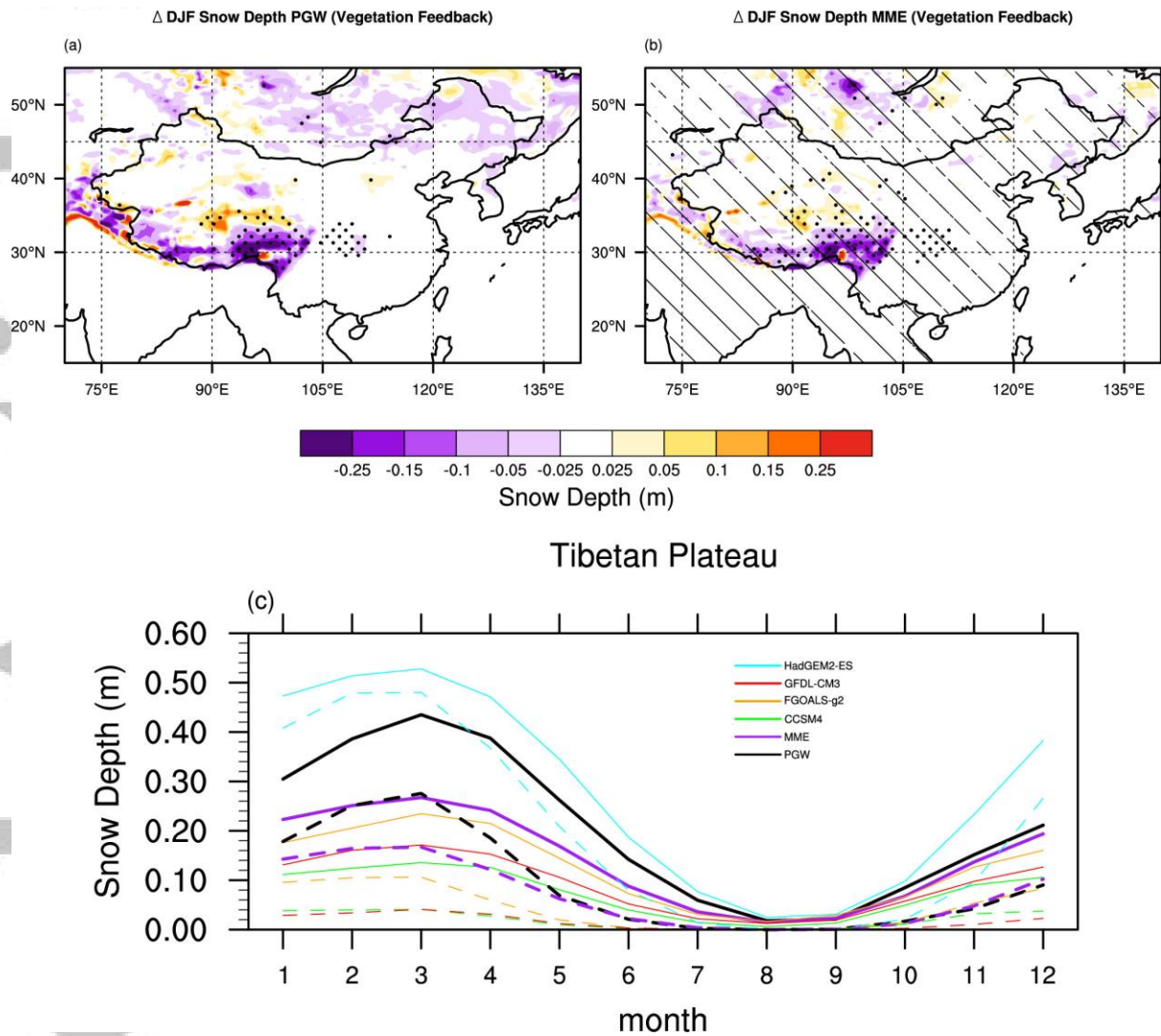


Figure 10. Impacts of vegetation feedback on (a-b) projected snow depth changes (units: m), and (c) projected snow depth changes averaged over Tibetan Plateau. The oblique lines indicate areas where 3 to 4 members agree with the MME results, and black dots indicate areas where the changes or differences pass the 5% significance test.